Analysis of convergent flow tracer tests in a heterogeneous sandy box with connected gravel channels

Antonio Molinari, Università della Calabria, Dipartimento di Ingegneria Civile, via P. Bucci 42B, 87036 Rende (CS), Italy (ant.molinari2002@libero.it),

D. Pedretti, Dept. of Earth, Ocean and Atmospheric Sciences, University of British Columbia, 2207 Main Mall, Vancouver, British Columbia, Canada V6T1Z4 (dpedretti@eos.ubc.ca),

C. Fallico, Università della Calabria, Dipartimento di Ingegneria Civile, via P. Bucci 42B, 87036 Rende (CS), Italy (carmine.fallico@unical.it)

Abstract. We analyzed the behavior of convergent flow tracer tests performed in a 3D heterogeneous sandbox in presence of connected gravel channels under laboratory-controlled conditions. We focused on the evaluation of connectivity metrics based on characteristic times calculated from experimental breakthrough curves (BTCs), and the selection of upscaling model parameters related to connectivity. A conservative compound was injected from several piezometers in the box and depth-integrated BTCs were measured at the central pumping well. Results show that transport was largely affected by the presence of gravel channels, which generate anomalous transport behavior such as BTC tailing and double peaks. Connectivity indicators based on BTC peak times provided better information about the presence of connected gravel channels in the box. One of these indicators, β, was defined as the relative temporal separation of the BTCs peaks from the BTCs centers of mass. The mathematical equivalence between β and the capacity coefficient adopted in mass-transfer-based formulations suggests how connectivity metrics could be directly embedded in mass-transfer formulations. This finding is in line with previous theoretical studies and was corroborated by reproducing a few representative experimental BTCs using a 1D semi-analytical bimodal solution embedding a mass-transfer term. Model results show a good agreement with experimental BTCs when the capacity coefficient was constrained by measured β. Models that do not embed adequate connectivity metrics or do not adequately reproduce connectivity showed poor matching with observed BTCs.

1. Introduction

Experimental studies conducted in the past demonstrated that aquifer heterogeneity generates anomalous (i.e., non Fickian) transport (e.g., [Becker and Shapiro, 2000; Boggs et al., 1992; Cortis and Berkowitz, 2004; Fernàndez-Garcia et al., 2002, 2004; Levy and Berkowitz, 2003; Meigs and Beauheim, 2001]). Since an exhaustive characterization of heterogeneity is generally not feasible at the scales controlling anomalous transport, tracer tests are performed at some metric scale and their results analyzed using integrated (upscaling) models. Among them, macrodispersive models or nonlocal formulations (e.g., [Dagan, 1989; Berkowitz et al., 2006; Benson et al., 2000; Haggerty and Gorelick, 1995]) have been successfully applied against experimental data (e.g., [Dagan, 1982; Levy and Berkowitz, 2003; McKenna et al., 2001; Sanchez-Vila and Carrera, 2004]).

These formulations, typically based on analytical or semi-analytical 1D solutions, are usually more practical than complex numerical models to reproduce anomalous transport. Yet, they are sometimes criticized since they can suffer from lack of a solid physical relationship between model parameters and aquifer properties, which impedes their use for predictive purposes (e.g., [Neuman and Tartakovsky, 2009]).

While most efforts were done to investigate such missing links under uniform flow configurations (e.g., [Willmann et al., 2008; Zinn and Harvey, 2003; Zhang et al., 2014]) significantly fewer studies focused on transport under forced-gradient convergent (FGC) flow. The latter is a widely adopted methodology to perform field-scale tracer tests (e.g., [Becker and Shapiro, 2000; Bianchi et al., 2011; Gutiérrez et al., 1997; Meigs and Beauheim, 2001; Ptak et al., 2004]), but requires more complex mathematical treatment for upscaling purposes than uniform flow transport. One reason is the lack of transport stationarity under radial flow [Matheron, 1967]. Fernàndez-Garcia et al. [2004] illustrated that parameters estimated using uniform flow tests substantially differ from those estimated under divergent or convergent flow. As such, basic processes controlling anomalous transport under FGC flow configuration are not yet completely linked to upscaling model parameters and require further investigation.

Recent theoretical studies indicate that anomalous transport under FGC flow is strictly related to mechanisms and concepts of connectivity, stratification, mixing and nonstationarity. Most of them also seem to be at the origin of anomalous transport under uniform flow conditions (e.g.,[Gomez-Hernandez and Wen, 1998; Sanchez-Vila et al., 1996; Willmann et al., 2008; Zinn and Harvey, 2003; Zhang et al., 2014]). Pedretti and Fiori [2013] used an analytical solution to show that anomalous scaling of BTCs is naturally associated with FGC flow in case of perfect transport stratification. Similar conclusions were drawn by Pedretti et al. [2013], who used numerical models to reproduce FGC tracer tests in synthetic fields. They observed that, after injecting at a distance of about one horizontal integral scale from the well in unconditional 3D Multi-Gaussian $\ln(K)$ fields (K being the hydraulic conductivity), depth-integrated BTCs displayed typical features associated with anomalous transport, such as nonsymmetrical shapes or tailing. Pedretti et al. [2013] associated this behavior to transport connectivity and stratification, as injected solutes moved preferentially through more permeable and well-connected layers rather than through less permeable and poorly-connected layers.

One consequence of tailing is the large separation of concentration peak time from the temporal scaling of the center of mass of a BTC. Pedretti et al. [2014] showed that, when properly normalized, this temporal lag is mathematically similar to the capacity coefficient (β) used in mass-transfer-based approaches. Indeed, the numerical simulations by Pedretti et al. [2014] performed in anisotropic Multi-Gaussian fields at various integer scales showed a high correlation between between BTC peak times and β; these authors proposed the existence of a physical link between β and connectivity based on the distribution of $\ln(K)$. These conclusions seem to be supported by other works based on uniform flow conditions. Zhang et al. [2014] performed synthetic tracer tests with larger injection scales than those reported by Pedretti et al. [2014], and conclude that a quantitative link between nonlocal parameters and aquifer heterogeneity may actually rely on the properties of highly-conductive materials, such as gravel channels.

Experimental studies supporting these hypotheses are lacking. Only a few experimental analysis addressed general aspect of the link between FGC transport parameterization and connectivity, without focusing on nonlocal parameters. Fernàndez-Garcia et al. [2004] used a 3D metric-scale box, characterized by anisotropic distribution of K clusters. They concluded that the presence of small connected paths may condition only specific transport parameters (e.g. apparent porosity), without affecting others (e.g. dispersivity). Similar conclusions were drawn from experiments performed at larger scales, such as the MADE site [Bianchi et al., 2011]. Macroscopic entities, such as gravel channels in less conductive sandy materials, are also associated with preferential transport and connectivity. This situation is typical of alluvial depositional systems and has a dramatic impact on the fate of flow and solutes in the subsurface, as the preferential paths may account for the majority of flow and consequently transport in the subsurface (e.g., [Labolle and Fogg, 2001; Rosqvist and Destouni, 2000]). Connectivity is a relatively new concept in hydrogeology; we refer to Renard and Allard [2013] for an extensive review of several static and dynamic connectivity metrics applied for the characterization of flow and transport in heterogeneous porous media.

The goal of our analysis is to provide experimental evidences to support theoretical studies dealing with anomalous transport in presence of FGC and to obtain additional insights about the missing link between anomalous transport, connectivity and model parameters under this flow configuration. For this purpose, multiple convergent flow tracer tests were repeated from different positions in a meter-scale physical box. The experimental setup focused on reproducing a naturally heterogeneous alluvial system where gravel channels are embedded in a finer sandy matrix. The analysis of experimental results consisted in two parts. First, we carefully analyzed the spatial distribution of connectivity indicators based on characteristic times from resulting depth-integrated BTCs. Then, we developed and used an upscaling solution based on a nonlocal effective model where β can be directly embedded as a model parameter. Representative experimental BTCs with different shapes and obtained from different injection locations in the box were used to compare the model-fitting ability of the nonlocal solution embedding β against models that did not embed connectivity, or models unable to reproduce anomalous transport. Other relevant aspects related to the model analysis, such as the mass transported in preferential channels compared to transport through sands, were also analyzed and discussed.

The paper is structured as follows. The experimental methodology (box setup and the execution of the tracer tests) is carefully described in Section 2. The dimensionless parameters and connectivity indicators used in the analysis are introduced in Section 3. The analysis of connectivity indicators obtained from the resulting BTCs is addressed in

Section 4. The model-based analysis is presented in Section 5. The paper ends with the main conclusions drawn from this work.

2. Experimental setup

2.1. Box description

The experimental box (Figure 1a) was constructed using a Plexiglass box to create a parallelepiped shape with the dimensions 144 cm x 60 cm x 60 cm (x,y,z). The system was equipped with two tanks connected to the public water network, which set constant hydraulic heads (CH) at two of the boundaries of the box. Water seeped from the lateral tanks into the porous system by means of perforated baffles located between the box and the tanks (Figure 1b).

The box consisted of 26 piezometers (pz) of 1 cm inner diameter, which acted as fully penetrating injection locations during the tracer tests. A borehole of 3 cm inner diameter, located in the center of the box, acted as a fully-penetrating pumping well during the tracer tests. Both the small piezometers and the large borehole were made of PVC perforated pipe and wrapped with a geotextile fabric. The fabric was used to avoid clogging of the perforated PVC by loose fine-grained material. However, the fabric space was sufficiently coarse to minimize the potential trapping of solute on the piezometer borders during tracer injection or within the well borders during the extraction.

A control tap, located under the central borehole, allowed dewatering of the system and creating the effect of a fully penetrating pumping well along the borehole column. Outlet water from the tap was collected in a storage tank where water could be sampled and tracer concentrations measured. Details about tracer tests compounds and measurement devices are provided in the next sections.

2.2. Characterization and distribution of geological materials

The sandbox was filled with two different inert materials, sand and gravel. To mimic a heterogeneous alluvial system where gravel channels are embedded by a finer hosting sandy matrix, the box was completed in the following steps (Figure 2a):

1. an initial 20-cm-thick layer of mixed fine to coarse sands was deposited on the bottom of the box. The average grain-size distribution (GSD) of this material, measured before setting up the box, ranged from 0.1 mm to 1 mm.

2. Layer 1 - several 3-cm-thick gravel packs were positioned on the top of the first sandy layer according to the spatial distribution depicted in Figure 2b and Figure 2d. The gravel GSD ranged from 2 mm to 10 mm. The remaining lateral spaces were filled with mixed sands;

3. a 15-cm-thick sandy material was deposited on top of Layer 1;

4. Layer 2 - another heterogeneous 3-cm-thick gravel-sandy layer was created similarly to Layer 1 (but with different spatial organization of gravels, as depicted in Figure 2c and Figure 2e);

5. a 10-cm-thick sandy material was deposited on top of Layer 2 to complete the box.

Full saturation conditions were achieved by flooding the box every 10 cm of additional material deposition and allowing degassing overnight. Hydraulic properties of sands and gravels prior deposition were determined using a Mariotte bottle, giving an approximate K range of $5 \cdot 10^{-2} - 10^{-1}$ m/d for sands and $10^{1} - 10^{2}$ m/d for gravels.

After the box was dismantled, several material samples were extracted from the system at random locations and used to measure in-situ GSD, K and porosity (ϕ). The (arithmetic) mean porosity of the system was estimated as $\phi = 0.31$. Sieve analysis showed that samples with larger proportions of gravel (i.e., those characterizing gravel channels) were approximately composed by 97% gravels and 3% sands. On the other hand, sandy samples (i.e., samples taken from the sandy matrix) were comprised of approximately 85% sands and 15% gravels. Constant-head permeability tests were repeated three times with three different hydraulic heads on each core, resulting in very similar K ranges as the loose material prior deposition. It was therefore assumed that the presence of isolated and unstructured gravel particles within the sandy matrix play a minor role on transport dynamics within the box, which was expected to be mostly controlled by the continuity of main connected gravel channels.

2.3. Resulting spatial organization of gravel channels

Due to the high contrasts in K, the resulting sandbox was considered to be hydraulically bimodal, with high K layers embedded in an overall lower K matrix. The spatial organization of material resulted into preferential channels (Figure 2), with different lateral continuity:

- Layer 1 (Figure 2d) consists of (a) a long, continuous gravel channel crossing the whole aquifer from the top-left corner to the opposite bottom-right corner, intercepting the well location; (b) a square, isolated gravel block (with an approximate planar size of 15 cm x 30 cm (x,y)) located near pz 1H and 2H; and (c) a short gravel channel (approximately 25 cm long), not intercepting the well.

- Layer 2 (Figure 2e) consists of three different gravel zones not intercepting the well: two continuous channels intercepting each other around pz 2G and one isolated gravel block located in the right side of the box, disconnected from the well by means of interposed sands.

2.4. Preparation and execution of the tracer tests

During the execution of the tracer tests, CH lateral boundary conditions were set to 55 cm and the bottom tap in the box was opened to reach a quasi-steady-state pumped equilibrium, with a final constant flow rate (Q) of about 0.05 L/s. In this configuration, head levels dropped by less than 25% of their initial values, which is within the limit of validity of the Boussinesq approximation for an unconfined aquifer to be analyzed as a confined aquifer [Bear, 1972].

A pulse injection of a known amount of mass was sequentially injected from each piezometer. The tracer was a saline solution of potassium iodide with concentration of $3 \cdot 10^{-3}$ M. The low reactivity of the solution allows for the assumption that the tracer behaved as a purely conservative compound in the system. Injections were performed manually with a needle and syringe to mimic a pulse injection. To ensure that the tracer was well mixed inside the piezometer column and to minimize any effects on the local flow regime, the needle was placed at the bottom of the piezometer and slowly lifted while continuously releasing the solute until the water table was reached.

After each injection, the conductivity of water drained from the system via the bottom tap was first measured using an electrode sensitive to iodide ions (Thermo Electron Corporation, 9653BN Orion Recorder, Iodide Electrode); this water was then discarded. Conductivity was converted to concentration values after the electrode was calibrated to known solutions of iodide. According to our calibration, the probe had a detection limit of 10^{-3} mg/L. Because of this low detection limit, the mass injected in a volume of 10 mL was sufficiently low to prevent large density contrasts and sufficiently large to be detected after being diluted in the well.

For each injection, concentration in the well was measured until 99% or more of the total injected mass was recovered. The tracer experiment was repeated for all of the 26 fully penetrating piezometers located at different positions from the central well and using the same boundary heads and pumping flow rate. After each injection, three to four pore volumes were pumped out of the system to prevent any interference between consecutive tracer experiments (i.e., to avoid detecting residual mass from the previous experiment).

3. Definition of connectivity indicators

We defined a series of dimensionless parameters and connectivity indicator used to analyze the behavior of solute transport in the heterogeneous box. The general idea was to analyze the departure of experimental BTCs from the corresponding behavior of an equivalent homogeneous domain (i.e., BTCs generated as if the same amount of solute mass had been injected in a homogeneous box under similar flow conditions).

We started considering that, under convergent transport taking place in a confined homogenous cylindrical aquifer of radius r and height b, the mean solute advection velocity (v) and advection time (τ) can be defined respectively as (e.g [Moench, 1989])

$$v(r) = \frac{Q}{2\pi r b \phi} \qquad \tau = \int \frac{\mathrm{d}r}{v(r)} = \frac{\pi r^2 b \phi}{Q}. \tag{1}$$

The variable τ, obtained after integration of v, represents a characteristic time which is usually adopted to normalize experimental BTCs under steady-state radial convergent flow. A normalization of the form $t_D = t/\tau$ (t_D being the dimensionless time and t the time) ensures that the center of mass of a depth-integrated BTC measured at the well (after a conservative tracer is injected as a pulse in a cylindrical homogeneous aquifer at a distance r from the well) scales at $t_D = 1$. The concentration peak time also scales at t_D=1 when $r/\alpha > 10$, where α is the longitudinal dispersivity [Moench, 1989].

The comparison of t_D with other characteristic times (T_i) obtained from BTCs can be used as an indicator of 'transport connectivity', i.e. a metric to evaluate the impact of connectivity on the behavior of solute plumes migrating in heterogeneous aquifers (e.g.,[Knudby and Carrera, 2006; Renard and Allard, 2013; Trinchero et al, 2008; Pedretti et al., 2014]). Under forced-gradient convergent transport, a set of connectivity indicators CI_i can be defined for instance as

$$CI_i = -\ln\left(\frac{T_i}{\tau}\right). \quad (2)$$

The larger CI_i the more 'connected' the injection and extraction points. Evaluating CI_i in correspondence of each injection location allows mapping the distribution of connectivity within the investigated domain. This approach was used by to analyze the impact of connectivity under radial convergent transport [Trinchero et al, 2008; Pedretti et al., 2014], and is adopted here for the analysis of connectivity in our experimental tracer tests.

Because of the boundary conditions affecting the flow field in the box, the aquifer departed from cylindrical conditions and (1) could not be directly applied to obtain τ. Indeed, the longest box sides acted as no-flow boundaries, while short sides acted as constant-head boundaries. To circumvent this problem, boundary-corrected advection times (τ') were evaluated numerically. The numerical approach consisted of two steps. First, a steady-state 2D flow simulation was carried out using MODFLOW [Harbaugh et al., 2000]. A uniform mesh discretization of 1 cm x 1 cm was adapted and boundary conditions similar to the box setup were implemented. The resulting flow field from the MODFLOW simulation was coupled with a particle-tracking code, RW3D [Fernàndez-Garcia et al., 2005] to obtain the advection time for each injection location. A classical exponential scheme for the interpolation of particle velocities was adopted.

In arbitrary flow fields, the simulated advection time depends directly on the hydraulic conductivity. For the sake of this analysis, the numerical simulation was performed assuming an isotropic, homogeneous hydraulic conductivity distribution with K=10 m/d. This value represents the lower limit of hydraulic conductivity measured in our box on such material (see Section 2). In this sense, the numerical simulation provides a distribution of minimum advection times associated with transport through gravel channels; as such, solute plumes moving faster than this advection time can be directly associated with transport through preferential channels. The importance of this specific selection can be readily understood from the definition of connectivity indicators hereafter.

Knowing τ', a boundary-corrected dimensionless time (t'_D) can be defined as

$$t'_D = \frac{t}{\tau'}. \tag{3}$$

A first indicator of transport connectivity (CI_1) can be obtained as

$$CI_1 = -\ln\left(\frac{\mu}{\tau'}\right) \tag{4}$$

where μ is the first temporal moment (center of mass) of the BTC resulting from the injection at a specific location. This is calculated as [Aris, 1956]

$$\mu = \frac{\int tC(t)\mathrm{d}t}{\int C(t)\mathrm{d}t} \tag{5}$$

where C is the measured concentration at the well. $CI_1 > 0$ indicates that, on average, the tracer mass moves faster in the box than in an equivalent homogeneous aquifer characterized by $K = 10$ m/d. In other words, a positive CI_1 would indicate that the center of mass of injected plumes would migrate according to the mean velocity of preferential gravel channels rather than the mean velocity of sands. Therefore, $CI_1 > 0$ indicates that transport between injection and extraction is directly controlled by the presence of preferential channels. On the other hand, a negative CI_1 would represent transport largely dominated by sands, as the center of mass would scale at later times than the minimum advection time for gravels. In this sense, CI_1 represents a direct physical measurement of connectivity associated with the impact of gravels on the average behavior of injected tracers.

A second indicator of transport connectivity (CI_2) can be defined from another characteristic time measured from BTCs, the concentration peak time (t_{pk}), as

$$CI_2 = -\ln\left(\frac{t_{pk}}{\tau'}\right). \tag{6}$$

In this case, $CI_2 > 0$ indicates that part of the injected mass is moving through preferential gravel channels, giving rise to the BTC peak earlier than the peak originated from transport through sands.

According to Pedretti et al. [2014], a third connectivity indicator could be determined by measuring the relative delay between the BTC peak time and the center of mass. This is defined as

$$\beta = \frac{\mu - t_{pk}}{t_{pk}}. \tag{7}$$

$\beta \to 0$ indicates that the peak time tends to correspond to the center of mass of solute distribution, which means a more symmetric distribution (similar, for instance, to the BTC observed under homogeneous conditions). On the other hand, a large β denotes that the center of mass is 'retarded' relative to transport through fast flow zones. This is similar to what described by mass-transfer formulations where the total retardation (R) caused by mass-transfer processes is computed as $R = 1 + \beta$ (e.g. [Haggerty and Gorelick, 1995]). Indeed, (7) is an approximation of the exact derivation of capacity coefficient from mass-transfer models [Pedretti et al., 2014]. Under FGC flow configurations, a larger retardation may occur when transport is more stratified and lateral connectivity is large [Pedretti et al., 2013]. Consequently, the capacity coefficient in nonlocal models could have a physical meaning associated with connectivity, and in turn transport connectivity can be directly embedded into mass-transfer formulations.

It should be noticed that, in multi-modal BTCs, multiple peaks exist and thus multiple β and CI_2 can be defined. The specific selection of the peak is very important to obtain an accurate indicator of connectivity and capacity coefficients, as discussed in the following. Indeed, these indicators may assume different values depending on the position of the selected peaks relative to the center of mass (e.g. $CI_2 >> CI_1$ and $\beta >> 0$ for highly positively skewed single-peaked BTCs).

4. Analysis of connectivity

We analyzed the impact of connectivity in our box by considering (1) the position of the peaks and the shape of the experimental BTCs, and (2) the values of connectivity indicators in each injection location based on characteristic times described in the previous section. Since the adopted indicators contain different information related to BTCs, it is worth analyzing which one provides greater ability to describe the impact of gravel channels on solute transport. We focused in detail on the ability of β to provide an accurate description of connectivity in the box, and infer if this indicator could be potentially used as an effective parameter in nonlocal formulations containing physical information regarding aquifer connectivity.

4.1. Qualitative aspects

Resulting BTCs from the experimental tracer tests are reported in Figure 3. In this plot, BTCs are normalized by the maximum concentration measured from each injection point (y-axes) and by t'_D (x-axes). Each sub-plot reports the group of BTCs associated with each injection line.

We observed that a few BTCs are characterized by double-peaked (bimodal) shape, with the first peak scaling at either $t'_D < 1$ (pz 1A , 3A, 1B, 3B, 2H, 3H and 3I) or $t'_D \approx 1$ (pz 2B, 1H, 2I). These BTCs correspond to injection points generally located far from the central well and in zones where gravel channels are elongated and laterally continuous from the top corners of the box to the well location. Because of the bimodal K distribution in the box, we can initially infer that bimodal BTCs arise due to a combination of transport through preferential gravel channels and the sandy matrix. The position of the first peak seems consistent with solute transport occurring preferentially through gravel channels and characterized by either $K = 10$ m/d (peaks scaling at $t'_D \approx 1$) or $K > 10$ m/d (peaks scaling at $t'_D < 1$). The second peak can be associated with transport in lower-conductive sandy materials, as these peaks generally scale at $t'_D > 1$.

A second group of BTCs was characterized by unimodal distributions, with the peak scaling at either $t'_D \approx 1$ (pz 3C, 3D, 2G, 3G, 1I), or $t'_D > 1$ (the remaining pz). These curves seem more symmetric than in the previous set of BTCs. Greater symmetry can be due to the proximity of these points to the well, as injected plumes may not sample sufficient heterogeneity to exhibit bimodal shape. Because of the adopted time normalization, single-peaked BTCs with peak scaling at $t'_D = 1$ reveal that transport from these locations may have occurred through gravel channels (contrarily, the peak would have scaled at $t'_D > 1$). Therefore, it seems that the presence of gravel channels may not be phenomenologically described from qualitative aspects such as modality and shape of the resulting BTCs. This result suggests that care must be taken when qualitative criteria regarding the BTC shapes are used to infer the impact of connected features or the presence of preferential channels in heterogeneous aquifers.

A more critical observation of these curves reveals indeed that the occurrence of gravel channels close to an injection location may not be a sufficient condition to generate bimodal BTCs associated to this injection point. The behavior of pz 2F and 3G is quite illustrative in this sense. These two injection locations are clearly close to a gravel channel, which seems apparently well connected and continuous from these injection points to the pumping well. The resulting BTCs do not display a double-peak behavior, while single-peaked BTCs are found instead. Remarkably, these BTC peaks scale at $t'_D > 1$, suggesting that transport from these two injected locations may have occurred almost exclusively through sands. This observation should warn decision makers about the use of 'static' (i.e. topologically-based, e.g. Renard and Allard [2013]) indicators to evaluate the impact of preferential channels on transport in heterogeneous porous media. From the behavior of pz 2F and 3G it seems that a clear link between topological indicators and the shape of BTCs may not be easily built for our box.

Another key aspect highlighted from this analysis concerns with the potential amount of mass migrating through preferential channels. We observed that a few double-peaked BTCs display peaks with very similar concentrations (e.g., pz 1I, 2I). This is true also for two other injection locations, pz 1A and 3I, although here slightly higher concentrations occur on the second peaks of the resulting BTCs. In contrast, other BTCs displayed markedly higher concentrations in one of the two peaks, preferentially the first peak (e.g., pz 3A, 3B, 3D, 2H) and in two cases the second peak (pz 1B, 3H). Larger concentrations on the first peaks are of great concern from a risk assessment perspective. They highlight that in some circumstances preferential gravel channels (associated with the first modes) can deliver a significant amount of mass along their pathways, despite being present in a few narrow channels. Preferential paths are not easily detected in routinely characterization practices, although they should constitute a primary goal for risk assessment of polluted aquifers [Trinchero et al, 2008].

4.2. Connectivity maps

Quantitative aspects of connectivity were inferred from the analysis of Figure 4, which reports the spatial distribution of the three connectivity indicators (CI_1, CI_2 and β), in correspondence of each injection location.

Figure 4-top illustrates the behavior of the connectivity indicator calculated using the temporal position of the BTCs center of mass (CI_1). It can be observed that this map does not display any specific spatial configuration; CI_1 is very homogeneously distributed and, remarkably, always found in the range $-2 < CI_1 < -1$. Negative CI_1 values indicate that the center of mass is retarded compared with the minimum advection time calculated for gravels, suggesting that the center of mass of injected solutes travels preferentially

according to the velocity of less-conductive sandy materials. This behavior is independent from the position of connected paths within the box, and seems to suggest that the first moment of solute travel times measured by depth-integrated BTCs may be insensitive to the presence of connected paths.

Figure 4-middle illustrates the distribution of connectivity indicators calculated using the BTCs peak times (CI_2). Black squares refer to indicators evaluated using the absolute peak times observed on the BTCs (i.e. the time associated with the maximum concentration measured for each BTC). This time refers to the first peak of all BTCs, except for pz 1A, 1B, 3H, 3I for which it refers to the second peak. This map shows significant variability among points, which span from negative values (the lowest being pz 1A, 1B, 3H, 3I) to positive values (the largest being 3A, 3B, 2H). Positive values suggest that part of the plume moved faster than the minimum advection time of gravels, indicating that BTCs peaks may be sensitive to the presence of channels and connected features. The apparently anomalous behavior of pz 1A, 1B, 3H, 3I is consistent with the fact that the second plumes do not actually represent transport through connected features in our box, but rather transport through less conductive sandy matrix. Indeed, larger values could be expected for these pz, which are located very close to a preferential channel. Results become more consistent when CI_2 is re-evaluated using the time scaling of the first peak. The new indicators (green squares in Figure 4-middle) assume now larger values, in line with other points where the presence of connected features affect transport.

Figure 4-bottom depicts the distribution of β, which reflects the apparent separation of mobile-immobile zones through the temporal delay BTC peaks from the BTC center of

mass. We observed that β is generally large ($\beta > 4$) around the well (e.g., pz 2F) and, at specific locations, far from the well (i.e., pz 2H, 3A and 3B).

Far from the well, large values of β are consistent with the presence of visible high K channels that have a strong impact on the transport. Indeed, as tracers move through these gravel zones, double-peaked BTCs were observed (pz 2H, 3A, 3B). Similarly to what was observed for CI_2, however, β is also influenced by a proper selection of a peak time representing transport through connected features. The behavior of pz 1A, 1B, 3H and 3I is again illustrative in this sense. At these locations β is quite low compared with other values in well-connected points. A larger β should be expected for these locations, as β should reflect the separation between the peak time and the center of mass associated with connected features (in agreement with the hypothesis by Pedretti et al. [2014]). Indeed, when β is calculated using the temporal scaling of the first peak instead of the second peak for pz 1A, 1B, 3H and 3I, the resulting values became larger (green triangles in Figure 4-bottom).

Close to the well, large β can be associated with the effects of plume's stratification and to the presence of small-scale features occurring in sands. Since injection-extraction distances are short, the presence of small-size heterogeneities (although not visually detected or easily measurable) may have a strong impact on arrival times of solutes at the well. When solutes tend to be perfectly stratified (which occurs when $r \to 0$), Pedretti and Fiori [2013] noted that BTCs can be highly positively skewed even for low hydraulic conductivity variance ($\ln(K) = 0.1$).

Our results suggest that connectivity can be better measured by indicators based on BTCs peak time, such as CI_1 and β, rather than those based on BTCs centers of mass.

This issue is promising for the potential use of β as an effective parameter to embed connectivity in nonlocal formulations. In fact, CI_1 and β provide similar information regarding transport connectivity in the box, and directly depends on the impact of gravel channels in the aquifer. Since β is mathematically equivalent to the capacity coefficient of mass-transfer formulations, the results suggest that β could be directly embedded in these models to upscale anomalous transport in alluvial settings associated with the impact of gravel channels. This conclusion is in line with the hypotheses by Pedretti et al. [2014] and Zhang et al. [2014].

We highlight however the key importance to evaluate adequate characteristic times related to connectivity. While in bimodal fields this characteristic time can be uniquely associated with the BTCs first peak, the presence of multiple peaks in multi-modal BTCs may hinder the presence of gravel channels. Hence, care must be taken when a clear link between BTCs peaks and connectivity may not be univocally established.

5. Effective transport modeling

To verify the potential use of β as an effective physically-based connectivity parameter in nonlocal formulations, we developed a semi-analytical bimodal model from the combination of two Moench's nonlocal solutions [Moench, 1995]. The bimodal model was used to fit selected single-peaked and double-peaked BTCs resulting from our experimental data sets after constraining the capacity coefficient term using measured β. The model analysis also provided an estimation of the amount of mass travelling through gravel channels compared with transport through sands, which is an important information to support decision making in risk assessment and remediation of polluted sites.

5.1. Model development

The bimodal semi-analytical upscaling model was obtained from the linear combination of two Moench's models. Each model is a 1-D advection-dispersion formulation in radial coordinates and characterized by single-rate spherical matrix diffusion term that simulates solute exchange between two regions: a region characterized by high advective transport, called here 'mobile' subdomain, and a region characterized by a larger porosity but with no advective transport, called here 'immobile' subdomain. The mobile subdomain is associated with a mobile porosity (ψ).

Assuming a pulse injection, negligible well radius and no retardation, the Moench's model is defined in the Laplace space as

$$\tilde{C}_i(s) = \exp\left(\frac{rG_i(\omega_i, s)}{2\alpha_i}\right) \tag{8}$$

where i refers to each of the two models ($i = 1, 2$), $\tilde{C}$ is the dimensionless concentration, s is the Laplace variable and G is a function of the parameter ω, defined in the Laplace space. The latter is defined as

$$\omega_i = \frac{2\alpha_i^2(s + q_i)}{r} \tag{9}$$

where q_i is the mass-transfer term, defined in the Laplace space. The last factor is defined upon three mass-transfer parameters (Table 1), known in Moench's terminology as matrix diffusion coefficient γ_i [-], fracture skin coefficient S_i [-], and storage coefficient ξ_i [-], the latter being similar to a capacity coefficient. Notice that this terminology is adapted to transport in fractured media, although the mathematical model is similar to conventional mass-transfer formulations (e.g., Carrera et al. [1998]). Setting $q = 0$ (no mass-transfer), the solution reduces to the classical ADE model solved in radial coordinates [Moench, 1989]. For additional details, such as the functional form of G, we refer to Moench [1995].

Moench's model is formulated in dimensionless concentration, $\tilde{C}$, and dimensionless time. The dimensionless concentration, $\tilde{C}$ is linked to dimensional variables as

$$C_i = \frac{\tilde{C}_i \pi r^2 b \psi_i}{M_i} \tag{10}$$

where M is the injected mass in each zone. Once $r, b, \psi, \tilde{C}$ are known (the latter estimated for instance by curve fitting), then the conversion from dimensionless to dimensional concentrations only depends on the injected M. A numerical inversion is required to solve for this model; we used the De Hoog algorithm [de Hoog et al., 1982] programmed in the MATLAB environment.

For each injection location, the dimensionless time was calculated using (3), which adopts a numerically calculated advection time to account for the impact of the boundary conditions on the box flow field. Note that in Moench [1995] the dimensionless time was calculated using the advection time τ defined in (1), since the original Moench's formulation applies to radial convergent transport and under the assumption of cylindrical aquifer conditions.

According to our experimental results, in some cases the injected solutes could generate bimodal plumes, with two characteristic modes associated with high K gravel zones (first modes) and the other related to lower K sandy zones (second modes). A simple bimodal transport model was therefore defined as a linear combination of two Moench models, such that

$$C = wC_1 + (1-w)C_2 \tag{11}$$

where w (formally known as a mixing parameter for binomial distributions) scales the contribution of each zone to the final BTC; w **varies in the range [0,1]**. The bimodal model is defined such that transport in each K zone is independent from the other and can be subjected to different mechanisms. For instance, one zone can display apparent mass-transfer-like mechanisms and thus be better fitted setting $q > 0$, while the other can behave as an ADE-like model and be better fitted by setting $q = 0$.

We tested the validity of the semi-analytical solution based on the Moench's model to a non-cylindrical domain using RW3D. The numerical testing framework was similar to the one adopted for the estimation of advection time (see Section 3), except that a larger number of particles was used and mass-transfer mechanisms were imposed on particle displacement. The implementation of mass-transfer mechanisms in RW3D is described in details in Fernàndez-Garcia et al. [2005]. Results (not reported) show perfect matching between the semi-analytical solution and the numerical results.

5.2. Model fitting procedure

To apply the model to fit the experimental BTCs, thirteen parameters are needed. The model requires six parameters for each zone (M_i, ψ_i, α_i,γ_i,S_i, ξ_i) and w. To model single-peaked BTCs the number of parameters needed was reduced to six, since $C_2 = 0$ and $w = 1$. While some parameters could be constrained to some physical properties and observed transport characteristics from the BTCs, others require calibration. In this framework the curve fitting procedure was developed according to the following main steps:

1. finding initial ADE-based parameters that visually matched specific parts of the BTCs;

2. optimizing selected initial parameters using a Monte Carlo Sensitivity Analysis (MCSA) choosing a range of values close to the initial ones;

3. finding initial ADE+MT values that visually match the entire BTC;

4. optimizing this second set of values by means of a new MCSA.

For step 1, initial values of ψ_i were approximated as $\psi_i \approx \psi_i^r = (Qt_{pk,i})/(\pi r^2 b)$, where $t_{pk,i}$ is the peak time of each BTC mode. This time roughly corresponds to the mobile advective time in multi-continuum formulations, and ψ^r is the mobile porosity under radial convergent transport (e.g., [Pedretti et al., 2014]). To obtain the initial values of α_i and $\tilde{C}_i$ for the first mode, it was assumed that the early-time behavior (rising part) of the first BTC mode would correspond to an ADE-like transport, and its concentration peak would correspond to the peak of the first mode. Thus, an ADE-like solution was used to visually fit the first mode and match α_1 and $\tilde{C}_1$. A similar procedure was followed for the second mode of double-peaked BTCs, but in this case α_2 and $\tilde{C}_2$ were visually fitted based on the late-time behavior (descending part) and concentration peak of the second mode.

Once ψ_i, α_i and $\tilde{C}_i$ were known, C_i only depend on the respective injected mass M_i and w. We noted from (11) that w was defined as a weight for C_1 and a complementary weight for C_2; since it must also hold that $M_2 = M - M_1$, it is easy to observe that w played the same role as M_1 and linearly scaled the amount of injected mass into each zone. As such, only one parameter between the M_1 and w needed to be calibrated; we decided to set w

= 0.5 and calibrate M_1. We could finally use (10) and (11) to transform $\tilde{C}_i$ into C_i and obtain C. The list of these initial values is reported in Table 1.

For step 2, a forward MCSA was applied to optimize the fitting parameters from step 1. Because of the low computation burden for each simulation, a large number of simulations were run ($n_s = 10^6$). The calibration was run twice to ensure convergence of MCSA was based on a selection of uniformly-distributed random parameters from a range of values close to the initially calibrated values. This was done to limit the degree of freedom of the sensitivity analysis and constrain the calibration to physically valid values close to the initial ones. Optimal values were determined as those generating the minimum root mean square errors (RMSE) between observed (C_{obs}) and simulated (C_{model}) concentrations. Log concentrations were used to further minimize the residuals across the BTCs early time and tails. Table 1 reports the optimized values, and the range of values used to generate the random distribution. RMSE was calculated as

$$\text{RMSE} = \sqrt{\frac{1}{n_s}\sum_{n=1}^{n_s}\left(\ln(C_{obs}) - \ln(C_{model})\right)^2}. \qquad (12)$$

Results from the initial calibration of four selected BTCs (Figure 5) highlighted that ADE models were in good agreement only with the early-time behavior of the first mode and with the late-time behavior of the second mode of double-peaked BTCs. ADE models largely underestimated the late-time behavior of the first mode and the early part of the second mode. As a result, the bimodal 1D ADE could not reproduce the intermediate behavior between the two modes, which is associated with stratification, connectivity and mixing of solute plumes at the pumping well when transported through zones characterized by different advective velocities and connectivity.

Because of tailing on the first modes, and assuming that transport in the experimental box could be effectively upscaled considering the presence of apparent mass-transfer-like mechanisms on transport through gravel channels, we imposed and calibrated $q > 0$ for model C_1. On the other hand, the satisfactory fitting of 1D ADE solution on the later part of the second modes suggests that the sandy material may not display these mass-transfer-like mechanisms. Consequently, we set $q = 0$ for model C_2.

We followed the hypothesis that the capacity coefficient could be exclusively controlled by the box connectivity, and that its impact on β may be known and measurable using (7). Thus, we did not optimized β via MCSA but imposed

$$\xi_1 = \psi_2 \beta. \tag{13}$$

This selection was done since β is typically defined as the ratio between immobile and mobile porosities. If the immobile porosity is defined as the difference between total porosity and mobile porosity, then the capacity coefficient would simply read $\beta = (\phi' - \psi)/\phi'$ and, using our notation, the Moench's storage coefficient ξ ([Moench, 1995], Table1) would read $\xi = (\phi' - \psi)\beta$ (note that they used $\psi = 1$). However, considering the work by Zinn and Harvey [2003], it is possible to hypothesize that multiple non-mobile regions may co-exist in the matrix, some of them effectively taking part in the mass-transfer process while some others (called 'no flow zones' in Zinn and Harvey [2003]) are not accessible to solute exchange. It is worth noticing that in Moench's work the amount $\phi' - \psi$ is defined as an 'interconnected porosity of the matrix', instead of immobile porosity. We thus decided to take the sandy matrix porosity ψ_2 as a representative value for an interconnected part of the matrix effectively taking part of the mass-transfer process, as sands contribute to transport processes as a less mobile region. This selection is discussed in the following part.

We finally considered that in Moench's solution mass-transfer occurs as matrix diffusion, while anomalous transport in our domain is mainly controlled by advection. As such, no clear link exists between mass-transfer rates and physical parameters controlling BTCs in our box, as aforementioned. Initial mass-transfer rates were thus arbitrarily set to $\gamma_1 = 0.05$ and $S_1 = 0.01$, similar to the values used by Moench [1995], and then refined using MCSA (Step 4).

5.3. Results and discussion

The model was applied to reproduce experimental BTCs from four selected injection locations in the box. These BTCs are illustrative of the salient patterns associated with the impact of channels on anomalous transport in our domain. In specific, we chose: a single-peaked BTC (pz 2A), a double-peaked BTC where the first peak has larger concentration than the second one (pz 3I), a double peaked BTC where the second peak has a significantly larger concentration than the first one (pz 3A) and a double-peaked BTC where the two peaks have comparable concentrations, although slightly larger for the first peak (pz 2I). In Figure 5, results from models embedding connectivity in the form of the nonlocal term (ADE+MT) are shown as blue dot-dashed lines, while those from models that do not embed connectivity (ADE) are reported as gray dotted lines. Observed BTCs are reported as red continuous lines.

We observe that the ADE+MT model provided a better match with observed values than ADE models for the four selected cases. This was also quantitatively confirmed by the lower RMSE computed from the model involving mass-transfer within the ADE solution. This is true not only for the intermediate behavior between the two peaks of pz 2I, 3I, 3A, but also for the behavior of single-peaked BTC. For double peaked BTCs, the good fitting of the first mode using the mass-transfer-based model is consistent with the hypothesis that large connectivity (dominant in gravel zones) is directly linked with the apparent separation between mobile and immobile zones. This behavior is explained considering that the 1D ADE-based solutions may not reproduce anomalous transport related to stratification and convolution of transport arriving at the controlling sections. ADE solutions may require higher dimensions (2D or 3D models) to this purpose, at the expense of additional numerical burden due to the increased dimensionality. On the other hand, the nonlocal term in 1D ADE+MT model (q_i) lumps together the effective processes generating tailing. Indeed, Willmann et al. [2010] suggested that q_i may be actually seen as an effective mixing term, which seems in line with the observations from our analysis.

The link between connectivity and apparent mass-transfer seems striking when analyzing the results associated with pz 3I. As discussed in Section 4, at this location the second peak displays larger concentrations and β has consequently a lower value, resulting in an underestimation of intermodal behavior and second peak by ADE+MT solutions. On the other hand, matching was improved when β was evaluated from the first peak and used in the ADE+MT solution (blue dot-dashed line); this was also confirmed by RMSE metrics. This issue provides support to the hypothesis proposed in this analysis, and further indicates that care must be taken when choosing the proper characteristic time to estimate β.

Effective upscaling formulations embedding connectivity metrics seem to provide more conservative estimations of solute transport than 1D ADE models. The estimated mass through the ADE+MT model significantly differed from the estimations based on the ADE model. More specifically, the 1D ADE solution largely underestimated transported mass in the high K zones compared to ADE+MT results. This is true for the three double-peaked BTCs reported in Figure 5. The best-fitting 1D ADE model predicted M1 = 0.09 - 0.21, while the ADE+MT predicted M1 = 0.40 - 0.72. Focusing on the pz 3A, M1 comprised more than 70% of the total injected mass according to the ADE+MT model, i.e. about 3 times larger than M1 evaluated on the basis of the classical ADE formulation.

In all cases investigated, calibrated parameters seem to be consistent with typical values encountered during tracer tests (Table 1). Optimized values were generally consistent with those obtained by visual matching, indicating the physical validity of the resulting estimated parameters. For instance, longitudinal dispersivity for sands is of the order of one tenth the injection-extraction distance; lower dispersion is associated with gravel materials, reflecting the lower tortuosity and larger connectivity sampled by solute plumes when migrating through gravel channels.

Similar considerations apply to mobile porosities ψ_i, which are also consistent with lower effective values for gravel and larger values for sands. From Table 1 we noted that the sum of ψ_1 and ψ_2 is not equal to the total aquifer porosity ($\phi = 0.31$). From one side, this is due to the elliptical distribution of advective porosity in the box; from another perspective, we can also consider the existence of no-flow zones that reduce the effective amount of interconnected porosity (actively contributing to the mass-transfer process), consistent with the work by Zinn and Harvey [2003].

Resulting mass-transfer rates γ_1 and S_1 significantly changed from initial estimating parameters to optimized values. This was somewhat expected since we used general parameters without a clear link to physical parameters. However, we observed that mass-transfer rates are quite similar among all injection locations showing double peaks (including the two different capacity coefficients used for pz 3I). This may indicate consistency between mass-transfer model parameters and physical properties of the aquifer, also related to connectivity, stratification and preferential transport through gravels. While the link is not mathematically known, our results are consistent with the conclusions achieved by Zhang et al. [2014], who associated subdiffusion in the gravel material as possible mechanism controlling mass-transfer rates.

We highlight that our semi-analytical solution accounts for single-rate mass transfer only. The use of more sophisticate models, such as a multi-rate model (e.g., Haggerty and Gorelick [1995]), should be able to enhance fitting of experimental BTCs, especially on tailings. We experienced difficulties in inverting the Laplace-based semi-analytical solution with multi-rate mass-transfer coefficients, and thus decided to limit our analysis to a single-rate model. Although not explored in detail, we argue that the selection of mass-transfer rate distribution should not alter our key conclusions. The link between capacity coefficient and physical connectivity is independent from the distribution of mass-transfer rates. Depending on the specific model formulation, multi-rate solutions involve a special function that spans mass-transfer rates according to some predefined distribution model. This function does not affect the total capacity coefficient, which is the same as in single-rate formulations (i.e., same total effective retardation $R = 1 + \beta$ for both formulations).

6. Conclusions

Adequate characterization and modeling of solute plumes migrating through preferential channels is of primary importance to make effective decisions in risk assessment and remediation of polluted aquifers. Preferential channels require special attention because of their erratic occurrence and uncertain detection, and the complex modeling of solute transport in heterogeneous porous media. This is especially true when upscaling solutions are applied to model forced-gradient tracer tests.

The primary goal of this work was to investigate if transport connectivity metrics can be used as physical constrains for nonlocal model parameters used to upscale transport under convergent flow configuration. For this purpose, we analyzed a series of tracer tests performed in an experimental sandbox characterized by known geometrical distribution of gravel features, hydraulic properties and controlled forced-gradient flow conditions.

We observed that on our box the presence of gravel channels within a sandy matrix strongly control characteristic patterns associated with anomalous transport, such as BTCs strong asymmetry, double peaks and tailing at late time. As tailing increases, the apparent separation of transport into mobile-immobile zones becomes more evident and connectivity metrics based on BTCs peak time become more directly related to the presence of gravel channels. Interestingly, the center of mass seems poorly affected by the presence of gravel channels, which indicate that indicators based on this time provide poor information about the presence of connected features.

Among the three connectivity indicators adopted in this work, the one based on the temporal separation between BTC peak and center of mass (β) was found to be an adequate parameter to detect and track the impact of gravel channels on solute transport. A larger degree of connectivity corresponded to a larger β, in agreement with the theoretical conclusions by Pedretti et al. [2013, 2014]. This result is also in line with the conclusions by Zhang et al. [2014].

Since β is mathematically similar to the capacity coefficient of mass-transport models, these results suggest that nonlocal model parameters can be directly linked with transport connectivity metrics measurable from field experiments. To quantitatively explore this issue, we applied an analytical model embedding connectivity indicators as capacity coefficients to fit four selected BTCs, and compared these results against a more simple 1D ADE solution. We showed that this methodology can provide not only good agreement between experimental and model-based BTCs, but also conservative estimation of mass transport in heterogeneous media affected by preferential channels. Indeed, 1D ADE solutions strongly underestimated mixing and the amount of transported mass along preferential channels compared with mass-transfer based solutions.

We therefore conclude that connectivity metrics could offer a physical key to link aquifer heterogeneity and upscaling parameters. This is strictly true, however, provided that the proper characteristic time associated with connectivity is identified. A comparison with a model where peaks related to connectivity are not correctly identified also suggests that an adequate time selection is strictly necessary in order to obtain a reliable estimation of a capacity coefficient. In the case of the bimodal BTCs reported in this work, connectivity characteristic times were clearly associated with the temporal scaling of the BTCs first peaks. However, care must be taken when a similar approach is adopted for multimodal BTCs, as the convolution of transport through different layers can hinder the proper selection of a representative time for connectivity.

7. Acknowledgments

The authors acknowledge S. Guzzi (Università della Calabria, Italy) for her valuable technical support during all experimental operations from the setup of the system to the execution of the tracer tests; Prof. D. Fernàndez-Garcia (UPC-Barcelona Tech, Spain) for providing the equipment needed for the tests, and T. Roetting (CSIC, Spain) for his useful initial suggestions and support to perform the experimental activities; the Associate Editor and three anonymous reviewers for their useful insights that helped improving this manuscript. The authors endorse AGU data policy. All the data and additional information used and cited in this paper can be provided by the corresponding author (D. Pedretti) at specific requests.

Figure 1. Description of the experimental apparatus. (a) Frontal view during filling operations; (b) final outline and tank components (1 tap water network; 2 flow control input valves; 3 lateral tanks; 4 sandbox; 5 wells tap; 6 measurement tank; 7 measurement probe; 8 datalogger; 9 PC recorder; 10 discharge tank; 11 piezometer; 12 pumping well.)

Figure 2. (a) Schematic stratigraphy and (b) (c) distribution of preferential channels in the box. Dimensions are expressed in cm. In (d) and (e) labels refers to the piezometers used as injection locations during the tracer tests.

Figure 3. BTCs resulting from tracer tests performed in the experimental box. For each injection location, concentration values are normalized by relative maximum concentrations and time axes are normalized by numerically-calculated, boundary-corrected advective travel times using homogeneous isotropic K=10 m/d.

Figure 4. Comparison of transport indicators, based on normalized BTC first moment (CI_1), normalized BTC peak time (CI_2), and relative spreading between peak and first moment (β). Green features denote connectivity indicators evaluated using the first time peak of the BTCs.

Figure 5. Comparison between observed BTCs, ADE and ADE+MT models (with a different selection of capacity coefficient for pz 3I) for four selected injection locations.

References

Aris, R., 1956. On the Dispersion of a Solute by Diffusion, Convection and Exchange between Phases. Proc R Soc Lond 252 (1271), 538–550.

Bear, J., 1972. Dynamics of fluids in porous media. Elsevier, New York.

Becker, M., Shapiro, A. M., 2000. Tracer transport in fractured crystalline rock: Evidence of nondiffusive breakthrough tailing. Water Resour. Res. 36, 1677–1686.

Benson, D. A., Wheatcraft, S. W., Meerschaert, M. M., 2000. The fractional-order governing equation of Lévy Motion. Water Resources Research 36 (6), 1413–1423.

Berkowitz, B., Cortis, A., Dentz, M., Scher, H., 2006. Modeling non-Fickian transport in geological formations as a continuous time random walk. Reviews of Geophysics 44, RG2003.

Bianchi, M., Zheng, C., Tick, G., Gorelick, S., 2011. Investigation of Small-Scale Preferential Flow with a Forced-Gradient Tracer Test. Ground Water 49 (4), 503–514.

Boggs, J. M., Young, S. C., Beard, L. M., Gelhar, L. W., Rehfeldt, K. R., Adams, E. E., 1992. Field study of dispersion in a heterogeneous aquifer: 1, Overview and site description. Water Resources Research 28 (12), 3281–3291.

Carrera, J. et al. 1998. On matrix diffusion: formulations, solution methods and qualitative effects. Hydrogeology Journal, 6 (1), 178–190.

Cortis, A., Berkowitz, B., 2004. Anomalous Transport in Classical Soil and Sand Columns. Soil Sci. Soc. Am. J. 68, 1539–1548.

Dagan, G., 1982. Stochastic modeling of groundwater flow by unconditional and conditional probabilities: 1. Conditional simulation and the direct problem. Water Resources Research 18 (4), 813–833.

Dagan, G., 1989. Flow and transport in porous formations. Springer-Verlag.

de Hoog, F. R., Knight, J. H., Stokes, A., 1982. An improved method for numerical inversion of Laplace transforms. S.I.A.M. J. Sci. and Stat. Comp. 3, 357–366.

Fernàndez-Garcia, D., Illangasekare, T. H., Rajaram, H., 2004. Conservative and sorptive forced-gradient and uniform flow tracer tests in a three-dimensional laboratory test aquifer. Water Resources Research 40, W10103.

Fernàndez-Garcia, D., Illangasekare, T. H., Rajaram, H., 2004. Differences in the scale dependence of dispersivity and retardation factors estimated from forced-gradient and uniform flow tracer tests in three-dimensional physically and chemically heterogeneous porous media. Water Resources Research 41, W03012.

Fernàndez-Garcia, D., Sanchez-Vila, X., Illangasekare, T. H., 2002. Convergent-flow tracer tests in heterogeneous media: combined experimental-numerical analysis for determination of equivalent transport parameters. Journal of Contaminant Hydrology 57 (1-2), 129 – 145.

Gomez-Hernandez, J. J., Wen, X.-H., Feb. 1998. To be or not to be multi-Gaussian? A reflection on stochastic hydrogeology. Advances in Water Resources 21 (1), 47–61.

Gutiérrez, M. G., Guimerà, J., de Llano, A. Y., Benitez, A. H., Humm, J., Saltink, M., Apr. 1997. Tracer test at El Berrocal site. Journal of Contaminant Hydrology 26 (14), 179–188.

Haggerty, R., Gorelick, S., 1995. Multiple-rate mass transfer for modeling diffusion and surface reactions in media with pore-scale heterogeneity. Water Resour. Res. 31 (10), 2383–2400.

Harbaugh, A. W., Banta, E. R., Hill, M. C., McDonald, M. G., 2000. MODFLOW-2000, the U.S. Geological Survey modular ground-water model User guide to modularization concepts and the Ground-Water Flow Process. Tech. rep., U.S. Geological Survey Open-File Report 00-92, 121 p.

Knudby, C., Carrera, J., 2006. On the use of apparent hydraulic diffusivity as an indicator of connectivity.. J Hydrol 2006;329(34):377-389.

LaBolle, E. M. and Fogg, G. E., 2001. Role of molecular diffusion in contaminant migration and recovery in an alluvial aquifer system. Transp Porous Media 42 155–179.

Levy, M., Berkowitz, B., Jul. 2003. Measurement and analysis of non-Fickian dispersion in heterogeneous porous media. Journal of Contaminant Hydrology 64 (34), 203–226.

Matheron, G., 1967. Elements Pour Une Theorie des Milieux Poreux. Masson et Cie, Paris.

McKenna, S. A., Meigs, L. C., Haggerty, R., 2001. Tracer tests in a fractured dolomite: 3. Double-porosity, multiple-rate mass transfer processes in convergent flow tracer tests. Water Resources Research 37 (5), 1143–1154.

Meigs, L. C., Beauheim, R. L., 2001. Tracer tests in a fractured dolomite: 1. Experimental design and observed tracer recoveries. Water Resources Research 37 (5), 1113–1128.

Moench, A. F., 1989. Convergent radial dispersion: A Laplace transform solution for aquifer tracer testing. Water Resour. Res. 25 (3), 439–447.

Moench, A. F., 1995. Convergent Radial Dispersion in a Double-Porosity Aquifer with Fracture Skin: Analytical Solution and Application to a Field Experiment in Fractured Chalk. Water Resources Research 31 (8), 1823–1835.

Neuman, S. P., Tartakovsky, D. M., 2009. Perspective on theories of non-Fickian transport in heterogeneous media. Advances in Water Resources 32 (5), 670–680.

Pedretti, D., Fernàndez-Garcia, D., Bolster, D., Sanchez-Vila, X., 2013. On the formation of breakthrough curves tailing during convergent flow tracer tests in three-dimensional heterogeneous aquifers. Water Resources Research 49 (7), 4157–4173.

Pedretti, D., Fiori, A., Oct. 2013. Travel time distributions under convergent radial flow in heterogeneous formations: insight from the analytical solution of a stratified model. Advances in Water Resources 60, 100–109.

Pedretti, D., Sanchez-Vila, X., , Fernandez-Garcia, D., Benson, D., Bolster, D., Fernandez-Garcia, D., 2014. Apparent directional mass-transfer capacity coefficients in three-dimensional anisotropic heterogeneous aquifers under radial convergent flow. Water Resour. Res., 50, 1205–1224.

Ptak, T., Piepenbrink, M., Martac, E., Jul. 2004. Tracer tests for the investigation of heterogeneous porous media and stochastic modelling of flow and transport - a review of some recent developments. Journal of Hydrology 294 (13), 122–163.

Renard, P., Allard, D., Jan. 2013. Connectivity metrics for subsurface flow and transport. Advances in Water Resources 51, 168–196.

Rosqvist, H. K., Destouni, G., Nov. 2000. Solute transport through preferential pathways in municipal solid waste. Journal of Contaminant Hydrology 46 (12), 39–60.

Sanchez-Vila, X., Carrera, J., 2004. On the striking similarity between the moments of breakthrough curves for a heterogeneous medium and a homogeneous medium with a matrix diffusion term. Journal of hydrology 294 (1-3), 164/175.

Sanchez-Vila, X., Carrera, J., Girardi, J. P., Aug. 1996. Scale effects in transmissivity. Journal of Hydrology 183 (12), 1–22.

Trinchero P, Sanchez-Vila X, Fernandez-Garcia D. Point-to-point connectivity, an abstract concept or a key issue for risk assessment studies? Adv Water Resour 2008;31(12):1742-53.

Willmann, M., Carrera, J., Sanchez-Vila, X., 2008. Transport upscaling in heterogeneous aquifers: What physical parameters control memory functions? Water Resour. Res. 44, W12437.

Willmann, M., Carrera, J., Sanchez-Vila, X., Silva, O., Dentz, M., 2010. Coupling of mass transfer and reactive transport for nonlinear reactions in heterogeneous media. Water Resources Research 46 (7).

Zhang, Y., Green, C. T., Baeumer,B., 2014. Linking aquifer spatial properties and non-Fickian transport in mobileimmobile like alluvial settings. Journal of Hydrology 512, 315–331.

Zinn, B., Harvey, C. F., 2003. When good statistical models of aquifer heterogeneity go bad: A comparison of flow, dispersion and mass transfer in connected and multivariate Gaussian hydraulic conductivity fields. Water Resources Research 39 (3), 1051.

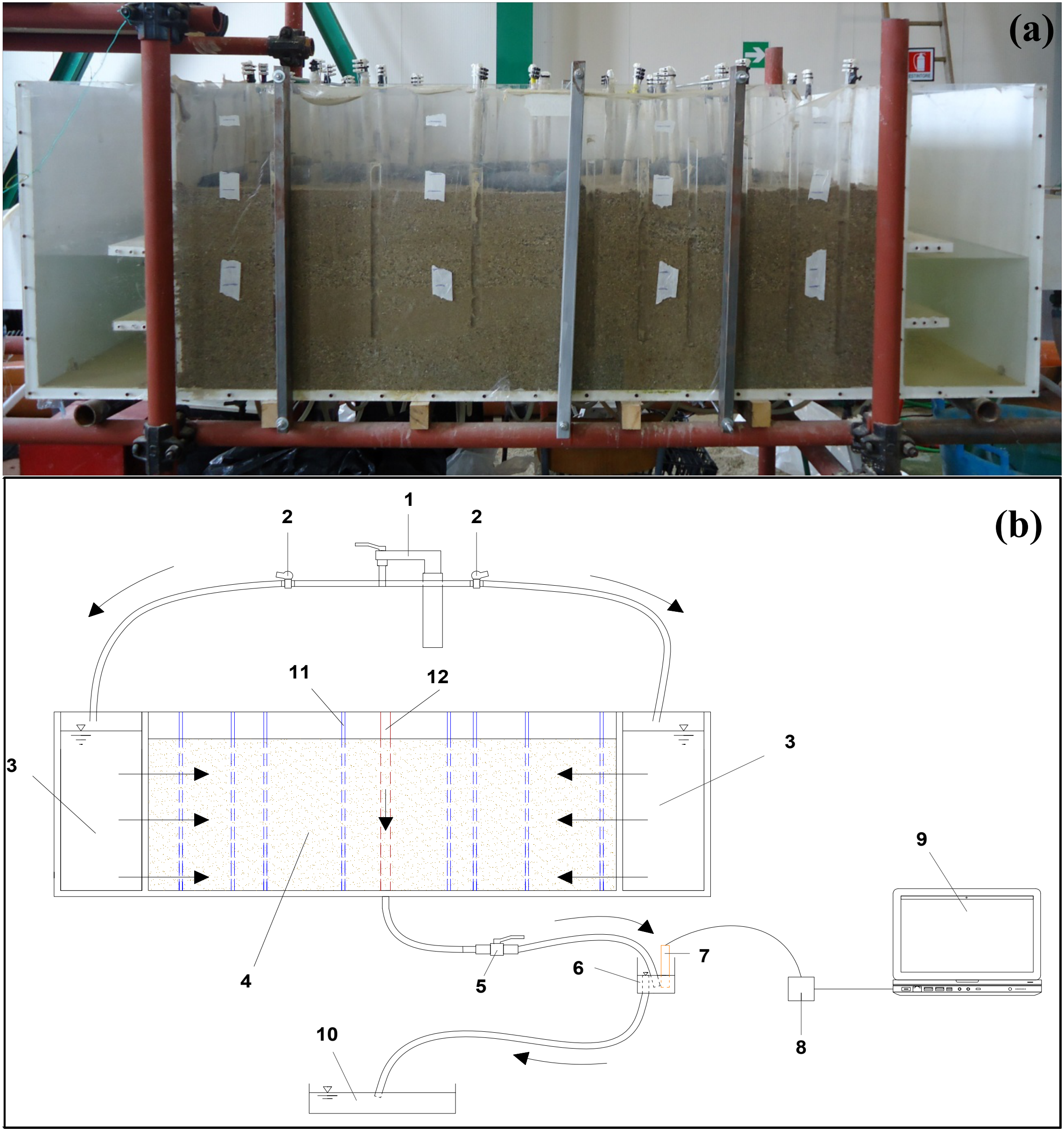
(a)
(b)
1
2
2
11
12
3
3
4
5
6
7
8
9
10

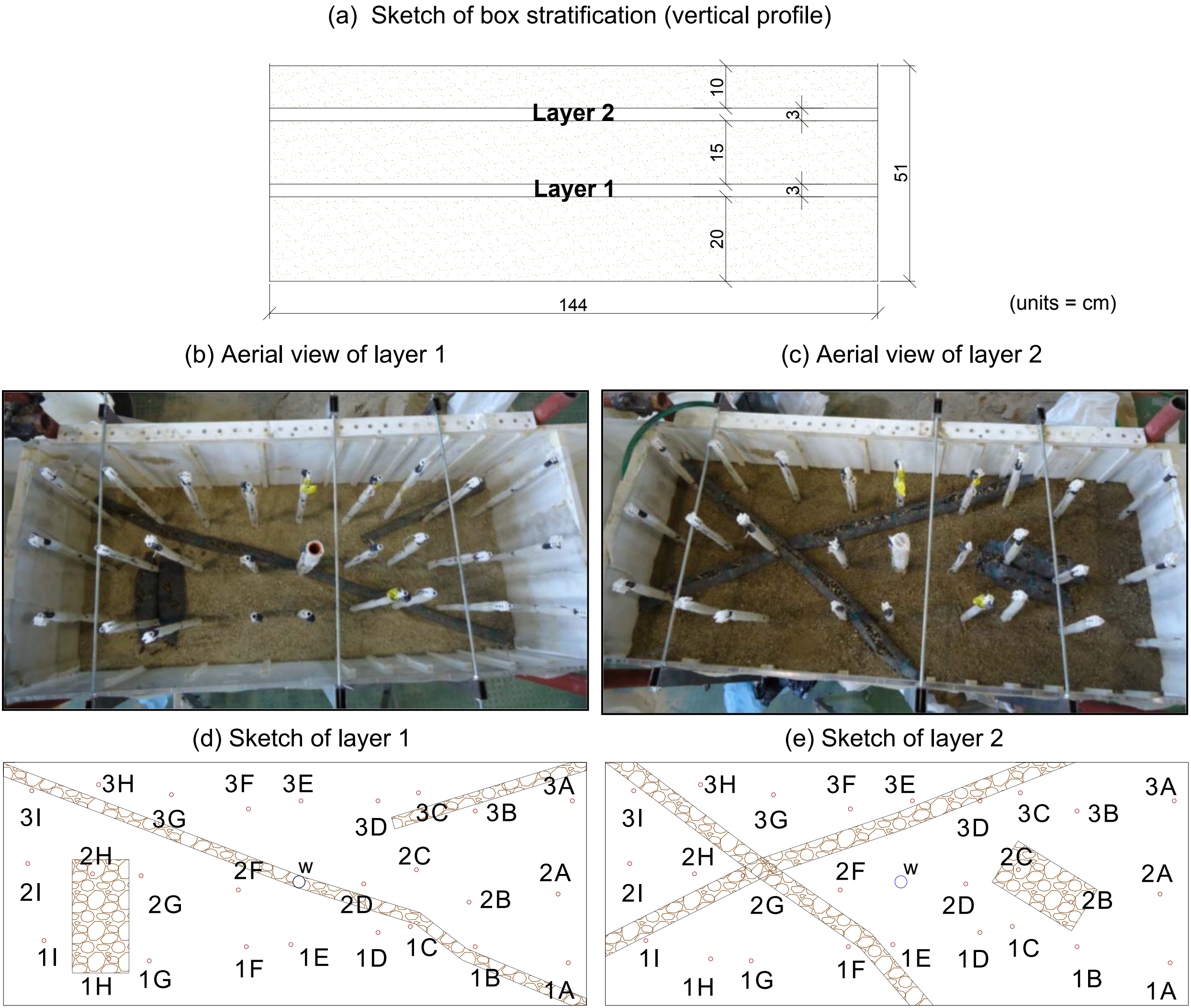
(a) Sketch of box stratification (vertical profile)
Layer 2
Layer 1
10
3
15
3
20
51
144
(units = cm)
(b) Aerial view of layer 1
(c) Aerial view of layer 2
(d) Sketch of layer 1
3H 3F 3E 3A
3I 3G 3D 3C 3B
2H 2C
2F w 2A
2I 2G 2D 2B
1I 1F 1E 1D 1C
1H 1G 1B 1A
(e) Sketch of layer 2
3H 3F 3E 3A
3I 3G 3D 3C 3B
2H 2C
2F w 2A
2I 2G 2D 2B
1I 1E 1D 1C
1H 1G 1F 1B 1A

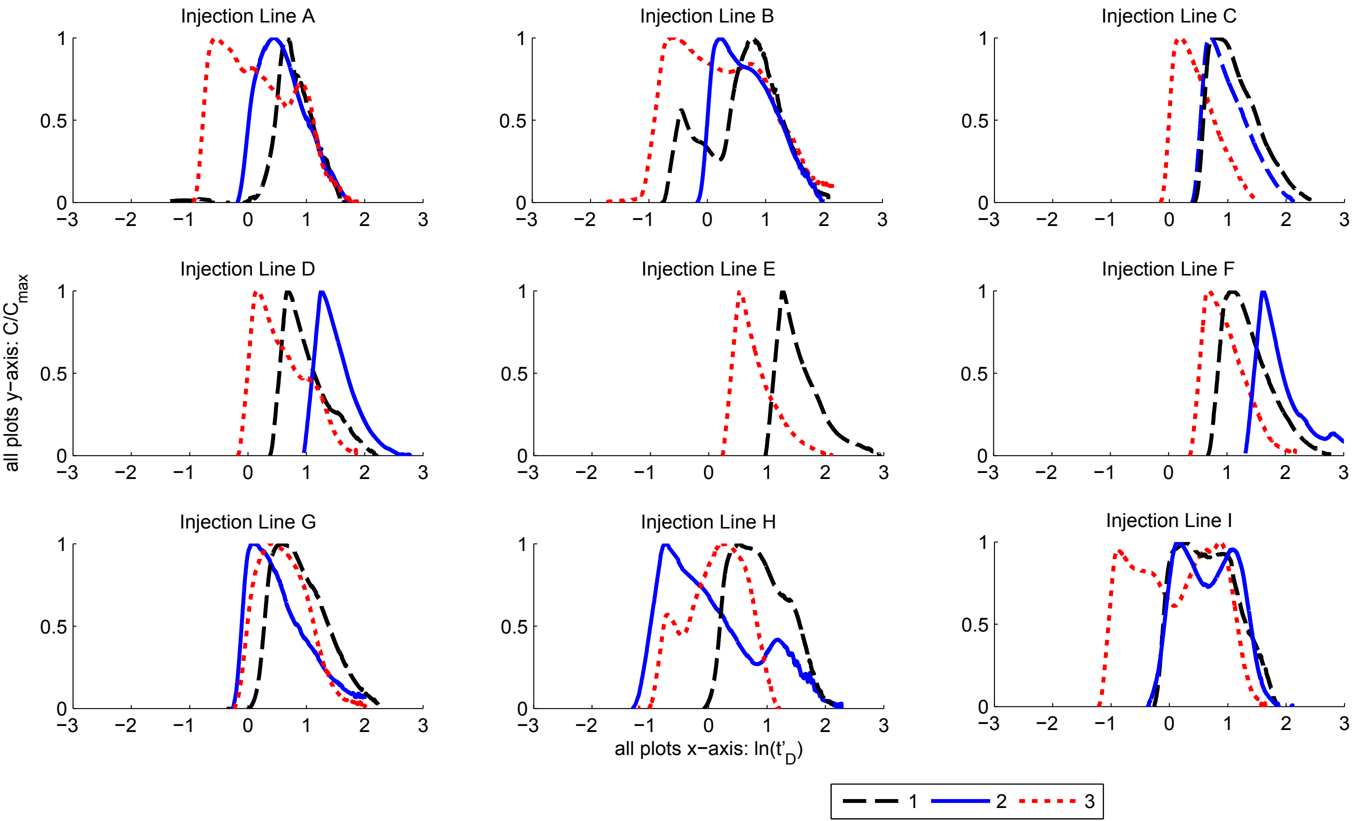
Injection Line A
Injection Line B
Injection Line C
Injection Line D
Injection Line E
Injection Line F
Injection Line G
Injection Line H
Injection Line I
all plots y−axis: C/C$_{max}$
all plots x−axis: ln(t'$_D$)
1
2
3

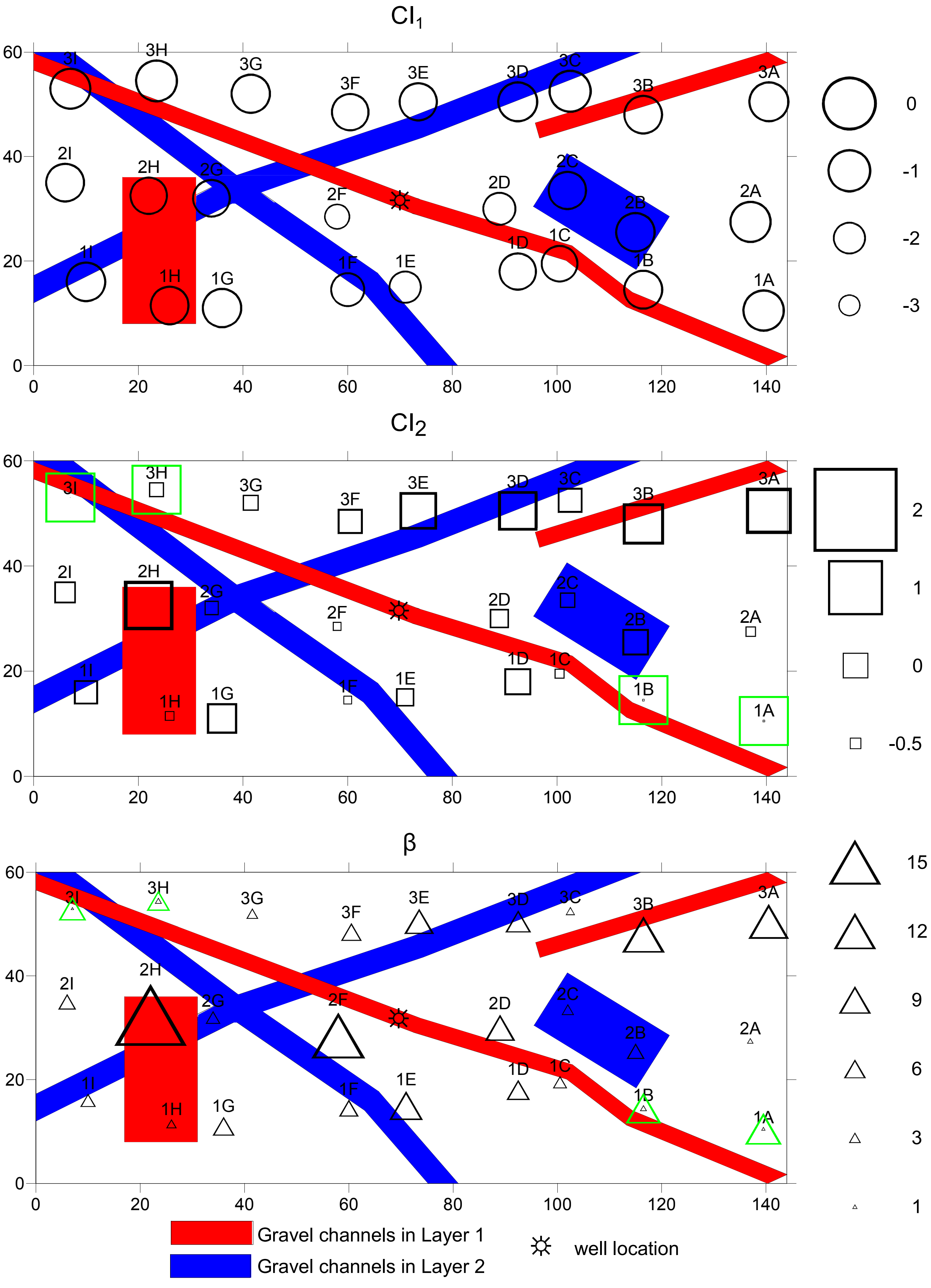
CI$_1$
CI$_2$
β
3I 3H 3G 3F 3E 3D 3C 3B 3A
2I 2H 2G 2F 2D 2C 2B 2A
1I 1H 1G 1F 1E 1D 1C 1B 1A
0
-1
-2
-3
2
1
0
-0.5
15
12
9
6
3
1
Gravel channels in Layer 1
Gravel channels in Layer 2
well location

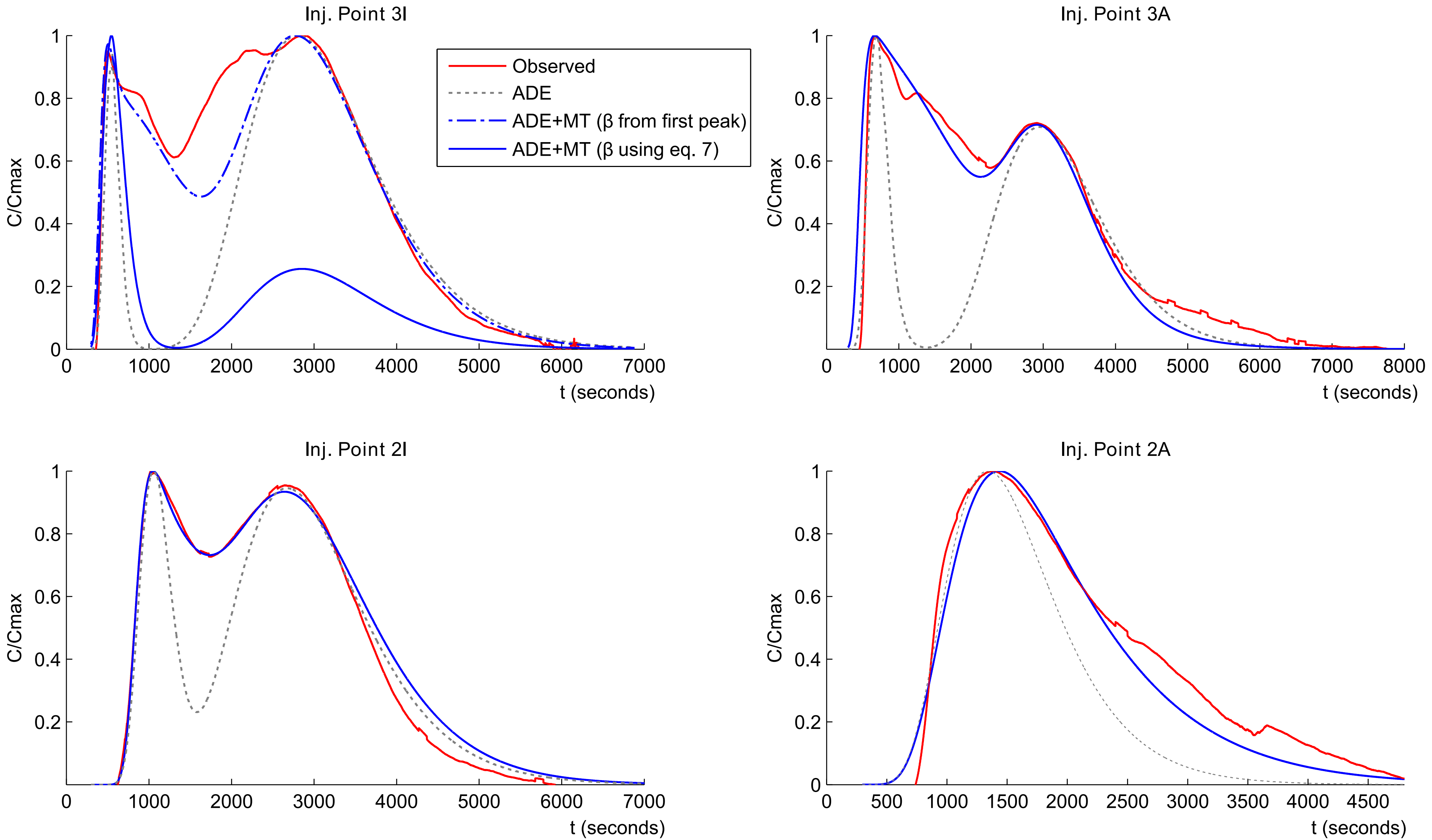

Inj. Point 3I
Observed
ADE
ADE+MT (β from first peak)
ADE+MT (β using eq. 7)
C/Cmax
t (seconds)
Inj. Point 3A
C/Cmax
t (seconds)
Inj. Point 2I
C/Cmax
t (seconds)
Inj. Point 2A
C/Cmax
t (seconds)